

Kosmotropic anion for improving cycling stability of aqueous lithium-ion batteries in salt-in-water electrolytes

Hyunjeong Oh

Korea Advanced Institute of Science and Technology

Seung-Jae Shin

Korea Advanced Institute of Science and Technology

Hirona Yamagishi

Ritsumeikan University

Toshiaki Ohta

Ritsumeikan University

Naoaki Yabuuchi

Yokohama National University <https://orcid.org/0000-0002-9404-5693>

Hyungjun Kim

Korea Advanced Institute of Science and Technology <https://orcid.org/0000-0001-8261-9381>

Hye Ryung Byon (✉ hrbyon@kaist.ac.kr)

Korea Advanced Institute of Science and Technology <https://orcid.org/0000-0003-3692-6713>

Article

Keywords: aqueous lithium-ion batteries, kosmotropic anions, LiCoO₂ electrode

Posted Date: May 19th, 2021

DOI: <https://doi.org/10.21203/rs.3.rs-525052/v1>

License:  This work is licensed under a Creative Commons Attribution 4.0 International License.

[Read Full License](#)

Abstract

The incompatibility between Li⁺-intercalated electrodes and water limits the practical feasibility of aqueous lithium-ion batteries (LIBs), which are economical and environmentally benign energy storage systems. Tremendous amounts of salts dissolved in water (water-in-salt) have been utilized to mitigate the access of water to the electrode/electrolyte interface and to extend the electrochemical potential window of aqueous LIBs. However, this approach has low viability owing to the expense of the salts. Here, we show that kosmotropic anions with moderate concentrations ($0.5 \sim 3 \text{ mol kg}^{-1}$) protect the LiCoO₂ electrode by harnessing water molecules. The sulfates of kosmotropic anions develop rigid water-solvation shells and also form ion pairs with Li⁺. All-atomic-level multiscale simulation revealed that sulfates tied with Li⁺ and the water shell are highly concentrated at the interface, thus decreasing the density of free water. The suppressed water activity explains the superior cell performance achieved with 0.5 mol kg⁻¹ sulfate relative to that in cells with 1 mol kg⁻¹ of chaotropic anions such as nitrate, perchlorate, and bis(trifluoromethylsulfonyl)imide. The formation of a liquid-phase protective layer is a new concept for developing stable aqueous batteries without the requirement for a solid-state electrolyte or an artificial protective layer on the electrode.

Introduction

With the increasing importance of safety, cost, and eco-friendliness, rechargeable batteries employing aqueous medium have received much attention as suitable for grid-scale energy storage systems (ESSs).¹⁻³ Aqueous lithium-ion batteries (LIBs) are one of the most feasible systems for industrialization as they can be promptly developed by transformation of well-established non-aqueous LIBs. However, most Li⁺-intercalating electrodes are incompatible with water, undergoing swift structural deformation, which results in poor cell performance.⁴⁻⁷ Recently, invaluable studies on water-in-salt electrolytes (WiSEs) have been demonstrated using very large amounts of bulky imide anions, such as 21 m (molal concentration, mol kg⁻¹) bis(trifluoromethylsulfonyl)imide (TFSI⁻) and additional bis(pentafluoroethylsulfonyl)imide.^{8,9,10} The limited free-water concentration and the formation of aggregated ion pairs in WiSEs alter the cell chemistry to establish a dense protective surface layer and widen the potential window.^{8,11-13} Nevertheless, utilizing WiSEs in practical aqueous LIBs is inexpedient because of the high cost of the large amount of salts and easy crystallization of the symmetrically structured anions.^{10,14,15}

Therefore, a more desirable approach is to maintain salt-in-water electrolytes and control the content of water and protons (H⁺), which are much more abundant than the electrolyte salts, to stabilize the Li⁺-intercalating electrodes. Water deforms the electrode surface chemically during cell operation.^{4,16} Furthermore, the dissociation of water produces H⁺, which is irreversibly inserted into the electrode structures and expedites capacity fading over a wide pH range.¹⁷⁻²¹ To curtail structural deformation of the electrodes, inorganic and graphitic protective layers have been introduced onto the electrode

surface.²²⁻²⁴ However, these solid-state layers may retard ion transport at the interface and generate cracks during cycling.

Instead, we herein introduce the new concept of a liquid-state protective layer formed with moderate concentrations (0.5 ~ 3 m) of anions. The key principle is to enhance the interaction of the anion with both water and Li⁺, and reduce the activity of free water molecules that are considered to be the source of H⁺. It is found that sulfate (SO₄²⁻), as a kosmotropic anion, mitigates the detrimental deformation of the lithium cobalt oxide (LiCoO₂, denoted as LCO) electrode. The rigid water structure formed adjacent to the kosmotropic anion aids in improving the cell cyclability. The structural details of the electrode-electrolyte interface are investigated using multiscale QM/MM simulations, revealing that the high charge density of the kosmotropic anion in the interfacial region induces localized concentration of the Li⁺ ions and lowers the free water density. In stark contrast, diffuse chaotropic anions such as TFSI⁻, nitrate (NO₃⁻), and perchlorate (ClO₄⁻) neither strongly controlled the water shell nor formed ion pairs. The resulting capacity fading with the chaotropic anions is in stark contrast with that of the kosmotropic system.

Results And Discussion

The galvanostatic cyclability of the LCO electrodes was first evaluated using two representative electrolyte salts, namely, 0.5 m Li₂SO₄ and 1 m LiTFSI, which both provided 1 m Li⁺. The LCO electrode with 0.5 m Li₂SO₄ exhibited a gradual increase in capacity at 0.5C over 30 cycles as the wetting of the electrode increased,⁵ and the coulombic efficiency (CE) approached 97% (**Figure 1a** and **1c**). By comparison, 1 m LiTFSI reduced the capacity from 110 to 30 mAh g⁻¹ (**Figure 1b**) and afforded an inferior CE of 94% (**Figure 1c**). Rate-capability tests with 1 m LiTFSI displayed an ill-defined capacity at various current rates (**Figure 1d**). In contrast, complete recovery of the capacity was found for the LCO electrode with 0.5 m Li₂SO₄ at the terminating 0.2C after 10C operation. These results reveal that the cyclability and rate capability of the LCO electrode are both anion-dependent.

To determine the origin of the capacity fading, the short-range order of the LCO structure was analyzed using soft X-ray absorption fine structure (XAFS) spectroscopy.⁷ In surface-sensitive partial electron yield (PEY) mode (< 10 nm depth), the Co³⁺ 3d-O 2p hybridization peak in the oxygen (O) K edge spectra (529.8 eV) was attenuated for both LCO electrodes after 30 cycles. In addition, a new signal emerged at 531.4 eV, attributed to partial oxidation of the lattice oxide of LCO; this signal is denoted as **O1** (**Figure 1e-f**).²⁵⁻²⁷ The **O1** signal was particularly intense for LCO with 1 m LiTFSI, indicating more extensive surface oxidation than in the case with 0.5 m Li₂SO₄. In bulk-sensitive partial fluorescence yield (PFY) mode (> 100 nm depth), the Co⁴⁺ 3d (t_{2g}⁵e_g⁰)-O 2p hybridization band was observed at 528 eV;²⁵⁻²⁷ this band is denoted as **O2** (**Figure 1f**). The signal was more pronounced with 1 m LiTFSI, consistent with a subtle shift of the main Co³⁺ signals to higher energy than others in the Co L₂ and L₃ edge spectra (**Figure S1**). Because the **O2** signal should disappear after Li⁺ intercalation during the discharging process, its existence after 30 cycles indicates incomplete Li⁺ intercalation into the LCO electrode. The remaining Li

vacancy and Co⁴⁺ cause local distortion of the octahedral CoO₆ unit.^{7,27} Long-range structural transformation was also observed. Powder X-ray diffraction analysis of the LCO electrode after operation with 1 m LiTFSI displayed split peaks related to the 003 reflection (**Figure S2**). The new peak appearing at 18.7° indicates widening of the interlayer distance due to the deficiency of Li⁺.^{4,28} In contrast, a less profound O2 signal was observed with 0.5 m Li₂SO₄ in the XAFS profile, along with a single 003 reflection, indicating complete Li⁺ intercalation into LCO after the same number of cycles.

Such inadequate Li⁺ intercalation has been ascribed to the insertion of H⁺ into the LCO electrode in previous studies.¹⁷⁻²⁰ H⁺ can be produced through the dissociation of water at the electrode surface in neutral or weakly alkaline solutions. Electrochemical impedance spectroscopy (EIS) can be used to distinguish Li⁺ intercalation and H⁺ insertion in the LCO electrode.¹⁹ Successive Nyquist plots were acquired at open-circuit potential (OCP, **Figure S3**), during the charging process (from 0.66 V to 0.8 V, red to yellow curves), and the discharging process (from 0.8 V to 0.63 V, light green to dark green curves) for three galvanostatic cycles (**Figure 2**). The emerging semicircle at the beginning of the 1st charge is attributed to the charge-transfer resistance of Li⁺ (R_{ct,Li^+}).^{19,20,29} The increased electronic conductivity of LCO decreased the semicircle size during the charging process, as a result of transformation from the semiconductor to the semi-metal by Li⁺ extraction.³⁰ During the discharging process, the semicircle gradually increased again with 0.5 m Li₂SO₄. Enlargement of the semicircle at the end of discharge (0.63 V) reflects Li⁺ filling at the topmost surface of the LCO electrode (**Figure 2a–b**).³¹ This behavior was repeated for all three cycles, and R_{ct,Li^+} was estimated as 27.8 Ω after 30 cycles (**Figure S4a** and **Table S1**). In comparison, the Nyquist plot of the LCO electrode with 1 m LiTFSI showed a larger semicircle corresponding to R_{ct,Li^+} at the beginning of the 1st charge (**Figure 2c–d**). More importantly, a new semicircle was observed in the low-frequency region at the terminal stage of the discharge process. Although this new semicircle vanished at the beginning of the following charging process over three cycles, it eventually grew irreversibly and accounted for a larger portion of the resistance (~147 Ω) after 30 cycles (**Figure S4b** and **Table S1**). This semicircle, which is apparently distinguished from that associated with R_{ct,Li^+} , is attributed to the resistance from H⁺ insertion (R_{ct,H^+}).^{19,20} The result of H⁺ insertion appeared at the end of the discharging process, that is, at the terminal stage of Li⁺ intercalation. This behavior was not observed with 0.5 m Li₂SO₄.

The intriguing question is which factor related to the electrolyte salt leads to the distinct degree of H⁺ insertion. Three possible factors were postulated: the pH, surface protective layer, and anion effects. The 1 m LiTFSI solution had a pH of 8, which is lower than that (pH 9.6) of the 0.5 m Li₂SO₄ solution (**Figure S5**). When the pH of the LiTFSI solution was adjusted to ~10 by adding LiOH, the capacity retention of LCO was still limited to ~34%, which is far inferior to the value of ~100% achieved with 0.5 m Li₂SO₄. The Nyquist plot for the LCO electrode with 1 m TFSI⁻ (pH 10) revealed suppression of H⁺ insertion in the 1st cycle (**Figure S6**). Nonetheless, the R_{ct,H^+} signal appeared at the end of the 3rd cycle (**Figure S6**), and both semicircles designated to R_{ct,Li^+} and R_{ct,H^+} grew over the course of 10 cycles (**Figure S7**), which is in line

with the capacity fading.³² In stark contrast, the $R_{ct,H+}$ signal did not appear for LCO with 0.5 m Li₂SO₄ at the 10th cycle, elucidating negligible capacity decay. Therefore, the pH effect was not critical under mildly alkaline conditions.

The formation of a solid-state protective layer on the LCO electrode was then considered. In non-aqueous media, decomposition of the electrolyte solution is accompanied by the construction of an interphase layer that serves to mitigate undesired surface reactions.^{33,34} However, both SO₄²⁻ and TFSI⁻ are inert in the given potential range. The X-ray photoelectron spectra (XPS) did not reveal any SO₄²⁻, TFSI⁻, or fragmental species of the electrolytes after 30 cycles (**Figure S8**). In the O 1s binding energy region, the signal of lattice Co–O at 529.7 eV was less intense, while the peak at 530.8 eV indicating both the oxide defects (O^{2+δ}) and the hydroxide became significant. This surface deformation was inevitably and chemically induced by the contact of the electrode with water, especially after Li⁺ extraction (**Figure S9**).^{4,6,16} Therefore, the above results indicate the absence of a solid-state protective layer over the LCO electrode. After 30 cycles, a thicker amorphous surface layer was formed on the LCO with 1 m LiTFSI, as observed in the transmission electron microscope images (**Figure S10**), demonstrating more acute surface degradation than that with 0.5 m Li₂SO₄.

Therefore, we focused on the last factor, the effect of the anion type. SO₄²⁻ and TFSI⁻ are well-known as strong kosmotropic and chaotropic ions, respectively, according to the Hofmeister series.³⁵⁻³⁸ Kosmotropic anions undergo intimate interactions with water and form a rigid solvation structure.^{39,40} In contrast, chaotropic anions, such as NO₃⁻, ClO₄⁻, and TFSI⁻, undergo weak interactions with water that induce disorder of the surrounding water structure. By investigating NO₃⁻ and ClO₄⁻ having less chaotropic character than TFSI⁻, the effect of the anions on the cell cyclability was elucidated (**Figure 3a–b**), where the molal concentration of all electrolyte salts was similar to the molar concentration (M, mol L⁻¹, **Table S2**). The LCO electrode with 0.5 m Li₂SO₄ showed ~73% capacity retention after 100 cycles. In comparison, 1 m LiNO₃ and 1 m LiClO₄ exhibited lower retentions of 33% and 13%, respectively. With the use of 1 m LiTFSI, the capacity decreased immediately after 30 cycles, and the CE of ~94% was lower than that (>99%) achieved with all other electrolytes. Consequently, the cell performance was very distinct and followed the order: SO₄²⁻ > NO₃⁻ > ClO₄⁻ > TFSI⁻, which corresponds to the reinforcing kosmotropic nature of the anion. Consistently, it appears to larger $R_{ct,Li+}$ of LCO with NO₃⁻ than that with SO₄²⁻ (**Figure S11a**). The presence of ClO₄⁻ promotes the formation of $R_{ct,H+}$ (**Figure S11b**). All these evidences support the decisive correlation between the surface reaction and cyclability.

The anion interaction perturbs the O–H vibrations of the water molecules, which are sensitive to the strength of the hydrogen bond. Infrared (IR) spectroscopy allows distinction of the vibrational bands of the O–H stretching at ~3200 cm⁻¹ for the strongest and ordered water structure versus that at ~3400 cm⁻¹ for the weaker hydrogen bond.⁴¹ When Li₂SO₄ was added to the water in concentrations from 0.1 to 3 m, the O–H band at ~3200 cm⁻¹ gradually intensified as the hydrogen-bond became stronger (**Figure**

3c). This result may be attributed to the Li^+ -water interaction, because the hydrogen bond of the water network is negligibly perturbed by SO_4^{2-} .⁴² In other words, the SO_4^{2-} -water interaction is as strong as the water network, thus providing a featureless signal. In sharp contrast, the IR band of LiNO_3 , LiClO_4 , and LiTFSI at $\sim 3200 \text{ cm}^{-1}$ became less intense in the order: $\text{NO}_3^- < \text{ClO}_4^- < \text{TFSI}^-$.^{41,43-45} This trend underpins the disordering of the solvation structure with increasing chaotropic nature of the anion. Additionally, the signals at $3500 \sim 3650 \text{ cm}^{-1}$ are related to both the free water and the chaotropic anion-water interaction.^{42,46-48} More pronounced absorption bands appeared at higher electrolyte concentrations, supporting the latter phenomenon. **Figure S12** shows different O-H vibrations depending on the anion type in the presence of 1 m Li^+ . Note that the range of influence of ions on the structure of water has been debated, from the first solvation shell to the mid/long-range hydrogen-bonding network.^{39,40,49} Nonetheless, it is generally agreed that the anions have profound impact on the closest water molecules, and the strength of their interactions in the first solvation shell can determine the macroscopic properties of the electrolyte solution.⁴⁰

More important is the effect of the anions on water structuring at the electrode surface, in accounting for the electrode deformation and the corresponding cell performance. The water structure in the bulk solution can be altered at the interfacial region by the local concentration of ions, surface charge of the electrode, material property, and applied electric field.^{50,51} The staircase-potential EIS in the non-faradaic potential region was quantified to electric double layer (EDL) capacitance (C_{dl}) on the LCO electrode (**Figure 4a** and **Figure S13**). In addition, the surface charge density (s) was calculated using Eq. 1 (**Figure 4b**):

$$\sigma = \int_{U^{\text{PZC}}}^U C_{\text{dl}}(U') dU' \quad (\text{Eq. 1})$$

where U is the electrode potential, and U^{PZC} is the potential at the point of zero charge (PZC) where C_{dl} approaches the minimum value. **Figure 4a** shows that the C_{dl} of 1 m LiTFSI is 1.5 ~ 3 times higher than the C_{dl} of the other electrolytes in the given potential range of $0.3 \sim -0.3 \text{ V}$ vs. Ag/AgCl. It is attributed to large van der Waals volume, high polarizability, and mild hydrophilicity of TFSI^- ,⁵²⁻⁵⁴ affording the excellent adsorption for both LCO material and carbon additive part in the EDL region (**Figure S14**). However, a higher C_{dl} does not necessarily mean a higher concentration of ion present at the “interface”, due to the possible formation of ion pairs. As the ion pairs do not contribute to the C_{dl} associated with the net surface charge, it is suggested to the necessity of full elucidation on the interfacial structure.

The detailed atomic arrangement of the interfacial structure formed at the LCO electrode was explicated using our recently developed mean-field QM/MM simulation.⁵⁵ To investigate the electrolyte response to the cathodic charging, two different surface charge densities of $s = 0$ and -11.5 mC cm^{-2} were compared. First, the local ion concentration along the surface normal direction (which was chosen as the

z-direction) revealed the formation of two layers within *ca.* 6 Å from the topmost atoms of the LCO electrode (**Figure S15a–b**). Additionally, the local water concentration also showed a layering tendency near the electrode surface, and then converged into the bulk value at $z > 6$ Å (**Figure S15c**). Thus, it is reasonably assumed that the region at $z < 6$ Å is an interfacial region, that is, a part of the EDL (nanometer scale) in direct contact with the solid electrode, at which the ion concentration and free water density were analyzed.

Figure 4c shows the number of anions located in the interfacial region when the aqueous electrolyte was interfaced with the LCO electrode. Notably, the local anion population near the electrode increased at $s = 0$ mC cm⁻² as the ion became more kosmotropic; SO₄²⁻ showed the largest population. A water adlayer was formed on the LCO surface (**Figure S16**), which can attract ions to the interfacial region via ion-dipole interactions. Because the ion-dipole interaction can be maximized for ions with a high charge density, kosmotropic ions such as SO₄²⁻ can accumulate in large quantities near the electrode surface.

Surprisingly, such a trend still holds even when the LCO electrode is cathodically polarized ($s = -11.5$ mC cm⁻²), where the anions experience electrostatic repulsion from the electrode (compare triangles and squares in **Figure 4c**). The LCO surface attracts Li⁺, which is further stabilized by the water adlayer (**Figure 4d**). In parallel, Li⁺ electrostatically attracts anions to form ion pairs. Kosmotropic anions having high charge density are now preferentially associated with small-size Li⁺ ions (**Figure 4e**), according to the “hard and soft acid and base (HSAB)” concept. The present simulation shows that contact ion pairs (CIPs) are more favorably formed when the anions have more kosmotropic character (**Figure S17**).

Along with the large increase in the local ion concentration (including Li⁺) with kosmotropic anions, the increased ionic strength near the electrode surface can minimize the number of uncoordinated water molecules, termed ‘free water’. This demonstrates the inverse relationship between the density of free water and the kosmotropic propensity of the anions (**Figure 4f**). Considering that the electrolyte pH is in the mildly alkaline range where water is regarded as the main H⁺ source, the lower free water density induced by the kosmotropic anions conceivably helps to suppress H⁺ insertion and maintain the stability of the electrode.

When the potential rose above 0.2 V, that is, positive *s*, the C_{dl} increased substantially for all electrolytes (**Figure 4a**) because many anions approach the EDL through electrostatic interactions. At 0.3 V, the *s* values for Li₂SO₄ and LiTFSI became comparable and were slightly higher than those of LiNO₃ and LiClO₄ (**Figure 4b**). The increased anion concentration can enhance the stability of the electrode against water, regardless of the anion type. It is demonstrated by the shift of the cutoff potential from -0.2 V to 0.3 V; the capacity retention was significantly increased from <35% to 56% with 1 m LiNO₃, 65% with 1 m LiClO₄, and 21% with 1 m LiTFSI over 200 cycles (**Figures S18–19** and **Table S3**). The cell with 0.5 m Li₂SO₄ still exhibited superior performance (67%) despite utilizing approximately half the concentration of the other anions. From the increasing C_{dl} at positive potential, we anticipate that the concentration of anions at the electrode surface would be similar for all electrolytes in the Faradaic potential region where

the Li^+ intercalation/extraction process occurs ($0.5 \sim 0.8$ V vs. Ag/AgCl). If Li^+ intercalation competes with H^+ insertion, a high Li^+ concentration near the LCO electrode is beneficial. Therefore, the ion pair formed by SO_4^{2-} is more likely to reduce the detrimental effect of water.

Based on the insights gained from the above studies, we attempted to improve the cell performance by increasing the concentration of SO_4^{2-} . The electrochemical potential window in the anodic region was slightly expanded with 3 m Li₂SO₄ (~ 130 mV, **Figure 5a**), implying that more SO_4^{2-} was localized on the electrode and suppressed the water reaction.^{8,56} The O–H vibration of 3 m Li₂SO₄ was analogous to that with 0.5 m Li₂SO₄ in the Raman and ATR-IR spectra (**Figure 3c** and **Figure S20**), while the symmetric SO_4^{2-} stretching mode in the Raman spectrum was blue-shifted at higher concentrations due to the significant formation of ion pairs (**Figure 5b**).^{57,58} Consistently, the appearance of an IR-inactive stretching band and the red-shift of the anti-symmetric SO_4^{2-} vibration evidenced the growing number of ion associations (**Figure S21**).⁴⁴

Full-cells composed of $\text{Li}_{9/7-x}\text{Nb}_{2/7}\text{Mo}_{3/7}\text{O}_2$ (LNMO) as the negative electrode, LCO as the positive electrode,^{59,60} and aqueous electrolyte solutions with different salt concentrations (0.5, 3 m Li₂SO₄, 1 and 3 m LiTFSI, and 9 m LiNO₃) were assembled. With the low-concentration electrolyte, LNMO limited the cell capacity to $40 \sim 90$ mAh g⁻¹_{LCO} (**Figure S22**). The 0.5 m Li₂SO₄ and 1 m LiTFSI-based full-cells both experienced rapid capacity fading over 50 cycles (**Figure 5c**) owing to the deformation of LNMO and the hydrogen evolution reaction in the salt-in-water system. In comparison, 3 m Li₂SO₄ delivered 74% capacity retention over 500 cycles, which is superior to that achieved with 3 m LiTFSI (38%) and 9 m LiNO₃ (34%) (**Figures 5c–d, Figure S23**, and **Table S4**). The outstanding cyclability attained using 3 m Li₂SO₄ is attributed to the extensive SO_4^{2-} -based liquid protective layer that harnesses the water molecules. Although the cells with 1 ~ 3 m LiTFSI exhibited higher initial capacity than those with the corresponding Li₂SO₄, prompt capacity fading was observed during cycling. In addition, the poor cyclability of 9 m LiNO₃ confirmed the indispensable role of the kosmotropic anions. Although the cell stability with the salt-in-water electrolyte is still inferior to that of WiSE (92% capacity retention with 21 m LiTFSI, **Figure S24**), this finding provides promise for developing aqueous LIBs with far lower electrolyte concentrations by tailoring the anion species.

In summary, we demonstrated the imperative role of anions in the salt-in-water electrolyte of aqueous LIBs. In the presence of chaotropic anions, severe capacity fading appeared due to deformation of the LCO surface by water and H^+ insertion. In contrast, sulfate, as a kosmotrope, mitigated these detrimental effects by establishing stronger sulfate-water and sulfate- Li^+ ion interactions. Atomic-scale multiscale simulations illuminated the higher local concentration of sulfate at the interfacial region of the LCO electrode. The stiff water structures and kosmotropic anion- Li^+ pairs generated a liquid-phase protective layer at the interface and alleviated the detrimental effect of free water molecules in deforming the electrode structure. This fundamental understanding sheds light on the mechanistics of the improved cell

cyclability with 0.5 m Li₂SO₄, providing 0.20% capacity-fading rate per cycle for 200 cycles in half-cells and 0.06% fading rate per cycle with 3 m Li₂SO₄ for 500 cycles in full-cells. The insight into the interfacial structure paves the way for the design of stable, inexpensive, and safe aqueous LIBs by tailoring the anion species and interfacial environments.

Declarations

SUPPLEMENTARY INFORMATION

Method, electrochemical and chemical analyses, details of computational data.

NOTES

The authors declare no competing financial interest.

ACKNOWLEDGMENT

This work was supported by the KAIST Global Singularity Research Program for 2021 and the National Research Foundation of Korea (NRF) grant funded by the Korea government (MSIT) (no. NRF2017R1A5A1015365). Soft XAS experiments were performed under the approval of the program committee (No. S17024, S18003, and S18030) of Ritsumeikan University.

References

1. Alias, N. & Mohamad, A. A. Advances of aqueous rechargeable lithium-ion battery: A review. *J. Power Sources* **274**, 237–251, (2015).
2. Wang, Y. G., Yi, J. & Xia, Y. Y. Recent Progress in Aqueous Lithium-Ion Batteries. *Adv. Energy Mater.* **2**, 830–840, (2012).
3. Eftekhari, A. High-Energy Aqueous Lithium Batteries. *Adv. Energy Mater.* **8**, 1801156, (2018).
4. Ramanujapuram, A. *et al.* Degradation and stabilization of lithium cobalt oxide in aqueous electrolytes. *Energy Environ. Sci.* **9**, 1841–1848, (2016).
5. Gordon, D. *et al.* Enhancing cycle stability of lithium iron phosphate in aqueous electrolytes by increasing electrolyte molarity. *6*, 1501805, (2016).
6. Byeon, P. *et al.* Atomic-scale observation of LiFePO₄ and LiCoO₂ dissolution behavior in aqueous solutions. *Adv. Funct. Mater.* **28**, 1804564, (2018).
7. Oh, H., Yamagishi, H., Ohta, T. & Byeon, H. R. Understanding the interfacial reactions of LiCoO₂ positive electrodes in aqueous lithium-ion batteries. *Mater. Chem. Front.* **5**, 3657–3663, (2021).

8. Suo, L. M. *et al.* "Water-in-salt" electrolyte enables high-voltage aqueous lithium-ion chemistries. *Science* **350**, 938–943, (2015).
9. Suo, L. M. *et al.* Advanced High-Voltage Aqueous Lithium-Ion Battery Enabled by "Water-in-Bisalt" Electrolyte. *Angew. Chem. Int. Ed.* **55**, 7136–7141, (2016).
10. Yamada, Y. *et al.* Hydrate-melt electrolytes for high-energy-density aqueous batteries. *Nat. Energy* **1**, 16129, (2016).
11. McEldrew, M., Goodwin, Z. A. H., Kornyshev, A. A. & Bazant, M. Z. Theory of the double layer in water-in-salt electrolytes. *J. Phys. Chem. Lett.* **9**, 5840–5846, (2018).
12. Vatamanu, J. & Borodin, O. Ramifications of Water-in-Salt Interfacial Structure at Charged Electrodes for Electrolyte Electrochemical Stability. *J. Phys. Chem. Lett.* **8**, 4362–4367, (2017).
13. Suo, L. M. *et al.* How Solid-Electrolyte Interphase Forms in Aqueous Electrolytes. *J. Am. Chem. Soc.* **139**, 18670–18680, (2017).
14. Wang, J. H. *et al.* Fire-extinguishing organic electrolytes for safe batteries. *Nat. Energy* **3**, 22–29, (2018).
15. Reber, D., Kuhnel, R. S. & Battaglia, C. Suppressing crystallization of water-in-salt electrolytes by asymmetric anions enables low-temperature operation of high-voltage aqueous batteries. *ACS Mater. Lett.* **1**, 44–51, (2019).
16. Motzko, M., Solano, M. A. C., Jaegermann, W. & Hausbrand, R. Photoemission Study on the Interaction Between LiCoO₂ Thin Films and Adsorbed Water. *J. Phys. Chem. C* **119**, 23407–23412, (2015).
17. Shu, Q., Chen, L., Xia, Y. Y., Gong, X. G. & Gu, X. Proton-Induced Dysfunction Mechanism of Cathodes in an Aqueous Lithium Ion Battery. *J. Phys. Chem. C* **117**, 6929–6932, (2013).
18. Gu, X. *et al.* First-principles study of H⁺ intercalation in layer-structured LiCoO₂. *J. Phys. Chem. C* **115**, 12672–12676, (2011).
19. Wang, Y. G., Lou, J. Y., Wu, W., Wang, C. X. & Xia, Y. Y. Hybrid aqueous energy storage cells using activated carbon and lithium-ion intercalated compounds - III. Capacity fading mechanism of LiCo_{1/3}Ni_{1/3}Mn_{1/3}O₂ at different pH electrolyte solutions. *J. Electrochem. Soc.* **154**, A228-A234, (2007).
20. Wang, Y. G., Luo, J. Y., Wang, C. X. & Xia, Y. Y. Hybrid aqueous energy storage cells using activated carbon and lithium-ion intercalated compounds II. Comparison of LiMn₂O₄, LiCo_{1/3}Ni_{1/3}Mn_{1/3}O₂, and LiCoO₂ positive electrodes. *J. Electrochem. Soc.* **153**, A1425-A1431, (2006).
21. Cherkashinin, G. & Jaegermann, W. Dissociative adsorption of H₂O on LiCoO₂ (00l) surfaces: Co reduction induced by electron transfer from intrinsic defects. *J. Chem. Phys.* **144**, 184706, (2016).
22. Tron, A., Jo, Y. N., Oh, S. H., Park, Y. D. & Mun, J. Surface Modification of the LiFePO₄ Cathode for the Aqueous Rechargeable Lithium Ion Battery. *ACS Appl. Mater. Interfaces* **9**, 12391–12399, (2017).
23. Zhi, J., Yazdi, A. Z., Valappil, G., Haime, J. & Chen, P. Artificial solid electrolyte interphase for aqueous lithium energy storage systems. *Sci. Adv.* **3**, e1701010, (2017).

24. Lee, H. J. *et al.* Off-Stoichiometry Induced Few-Nanometer Surface Layer for High-Performance Layered Cathode in Nonaqueous and Aqueous Electrolytes. *ACS Appl. Energy. Mater.* **1**, 5726–5734, (2018).
25. Mizokawa, T. *et al.* Role of oxygen holes in Li_xCoO_2 revealed by soft x-ray spectroscopy. *Phys. Rev. Lett.* **111**, 056404, (2013).
26. Chen, C. H. *et al.* Soft X-ray absorption spectroscopy studies on the chemically delithiated commercial LiCoO_2 cathode material. *J. Power Sources* **174**, 938–943, (2007).
27. Yoon, W. S. *et al.* Oxygen contribution on Li-ion intercalation-deintercalation in LiCoO_2 investigated by O K-edge and Co L-edge X-ray absorption spectroscopy. *J. Phys. Chem. B* **106**, 2526–2532, (2002).
28. Liu, L. J. *et al.* Electrochemical and in situ synchrotron XRD studies on Al_2O_3 -coated LiCoO_2 cathode material. *J. Electrochem. Soc.* **151**, A1344-A1351, (2004).
29. Bredar, A. R. C., Chown, A. L., Burton, A. R. & Farnum, B. H. Electrochemical Impedance Spectroscopy of Metal Oxide Electrodes for Energy Applications. *ACS Appl. Energy. Mater.* **3**, 66–98, (2020).
30. Menetrier, M., Saadoune, I., Levasseur, S. & Delmas, C. The insulator-metal transition upon lithium deintercalation from LiCoO_2 : electronic properties and ${}^7\text{Li}$ NMR study. *J. Mater. Chem.* **9**, 1135–1140, (1999).
31. Nakayama, M., Ikuta, H., Uchimoto, Y. & Wakihara, M. Study on the AC impedance spectroscopy for the Li insertion reaction of $\text{Li}_x\text{La}_{1/3}\text{NbO}_3$ at the electrode-electrolyte interface. *J. Phys. Chem. B* **107**, 10603–10607, (2003).
32. Lee, S. W. *et al.* The Nature of Lithium Battery Materials under Oxygen Evolution Reaction Conditions. *J. Am. Chem. Soc.* **134**, 16959–16962, (2012).
33. Schulz, N., Hausbrand, R., Wittich, C., Dimesso, L. & Jaegermann, W. XPS-Surface Analysis of SEI Layers on Li-Ion Cathodes: Part II. SEI-Composition and Formation inside Composite Electrodes. *J. Electrochem. Soc.* **165**, A833-A846, (2018).
34. Zhang, J. N. *et al.* Dynamic evolution of cathode electrolyte interphase (CEI) on high voltage LiCoO_2 cathode and its interaction with Li anode. *Energy Storage Mater.* **14**, 1–7, (2018).
35. Zhang, Y. J. & Cremer, P. S. Interactions between macromolecules and ions: the Hofmeister series. *Curr. Opin. Chem. Biol.* **10**, 658–663, (2006).
36. Reber, D., Grissa, R., Becker, M., Kuhnel, R. S. & Battaglia, C. Anion Selection Criteria for Water-in-Salt Electrolytes. *Adv. Energy Mater.* **11**, 2002913, (2021).
37. Lim, J. *et al.* Nanometric Water Channels in Water-in-Salt Lithium Ion Battery Electrolyte. *J. Am. Chem. Soc.* **140**, 15661–15667, (2018).
38. Su, H. L., Lan, M. T., Lin, K. W. & Hsieh, Y. Z. J. E. Chaotropic salts: Novel modifiers for the capillary electrophoretic analysis of benzodiazepines. *Electrophoresis* **29**, 3384–3390, (2008).
39. Schwierz, N., Horinek, D., Sivan, U. & Netz, R. R. Reversed Hofmeister series-The rule rather than the exception. *Curr. Opin. Colloid Interface Sci.* **23**, 10–18, (2016).

40. Omta, A. W., Kropman, M. F., Woutersen, S. & Bakker, H. J. Negligible effect of ions on the hydrogen-bond structure in liquid water. *Science* **301**, 347–349, (2003).
41. Kitadai, N. *et al.* Effects of ions on the OH stretching band of water as revealed by ATR-IR spectroscopy. *J. Solut. Chem.* **43**, 1055–1077, (2014).
42. Liu, J. H., Zhang, Y. H., Wang, L. Y. & Wei, Z. F. Drawing out the structural information of the first layer of hydrated ions: ATR-FTIR spectroscopic studies on aqueous NH_4NO_3 , NaNO_3 , and $\text{Mg}(\text{NO}_3)_2$ solutions. *Spectroc. Acta Pt. A-Molec. Biomolec. Spectr.* **61**, 893–899, (2005).
43. Cheng, F. Q. *et al.* FTIR analysis of water structure and its influence on the flotation of arcanite (K_2SO_4) and epsomite ($\text{MgSO}_4 \cdot 7\text{H}_2\text{O}$). *Int. J. Miner. Process.* **122**, 36–42, (2013).
44. Wei, Z. F., Zhang, Y. H., Zhao, L. J., Liu, J. H. & Li, X. H. Observation of the first hydration layer of isolated cations and anions through the FTIR-ATR difference spectra. *J. Phys. Chem. A* **109**, 1337–1342, (2005).
45. Chen, Y., Zhang, Y. H. & Zhao, L. J. ATR-FTIR spectroscopic studies on aqueous LiClO_4 , NaClO_4 , and $\text{Mg}(\text{ClO}_4)_2$ solutions. *Phys. Chem. Chem. Phys.* **6**, 537–542, (2004).
46. Dubouis, N. *et al.* The role of the hydrogen evolution reaction in the solid-electrolyte interphase formation mechanism for "Water-in-Salt" electrolytes. *Energy Environ. Sci.* **11**, 3491–3499, (2018).
47. Lee, M. H. *et al.* Toward a low-cost high-voltage sodium aqueous rechargeable battery. *Mater. Today* **29**, 26–36, (2019).
48. Cammarata, L., Kazarian, S. G., Salter, P. A. & Welton, T. Molecular states of water in room temperature ionic liquids. *Phys. Chem. Chem. Phys.* **3**, 5192–5200, (2001).
49. O'Brien, J. T., Prell, J. S., Bush, M. F. & Williams, E. R. Sulfate Ion Patterns Water at Long Distance. *J. Am. Chem. Soc.* **132**, 8248–8249, (2010).
50. Kasuya, M. *et al.* Anion Adsorption on Gold Electrodes Studied by Electrochemical Surface Forces Measurement. *J. Phys. Chem. C* **120**, 15986–15992, (2016).
51. Sverjensky, D. A. & Fukushi, K. Anion adsorption on oxide surfaces: Inclusion of the water dipole in modeling the electrostatics of ligand exchange. *Environ. Sci. Technol.* **40**, 263–271, (2006).
52. Bhattacharjee, S. & Khan, S. The wetting behavior of aqueous imidazolium based ionic liquids: a molecular dynamics study. *Phys. Chem. Chem. Phys.* **22**, 8595–8605, (2020).
53. Gorska, B., Timperman, L., Anouti, M. & Beguin, F. Effect of low water content in protic ionic liquid on ions electrosorption in porous carbon: application to electrochemical capacitors. *Phys. Chem. Chem. Phys.* **19**, 11173–11186, (2017).
54. Chiang, C. H., Chen, C. C., Nazeeruddin, M. K. & Wu, C. G. A newly developed lithium cobalt oxide super hydrophilic film for large area, thermally stable and highly efficient inverted perovskite solar cells. *J. Mater. Chem. A* **6**, 13751–13760, (2018).
55. Lim, H. K., Lee, H. & Kim, H. A Seamless Grid-Based Interface for Mean-Field QM/MM Coupled with Efficient Solvation Free Energy Calculations. *J. Chem. Theory Comput.* **12**, 5088–5099, (2016).

56. Zheng, J. X. *et al.* Understanding Thermodynamic and Kinetic Contributions in Expanding the Stability Window of Aqueous Electrolytes. *Chem* **4**, 2872–2882, (2018).
57. Rull, F. & Ohtaki, H. Raman spectral studies on ionic interaction in aqueous alkali sulfate solutions. *Spectroc. Acta Pt. A-Molec. Biomolec. Spectr.* **53**, 643–653, (1997).
58. Rull, F. Raman-spectroscopic study of the ion association of lithium-sulfate aqueous-solutions. *Z. Naturfors. Sect. A-J. Phys. Sci.* **50**, 292–300, (1995).
59. Hoshino, S. *et al.* Reversible three-electron redox reaction of Mo³⁺/Mo⁶⁺ for rechargeable lithium batteries. *ACS Energy Lett.* **2**, 733–738, (2017).
60. Nitta, K., Sakai, S., Fukunaga, A., Okuno, K. & Yabuuchi, N. (US Patent App. 16/494,080, 2020).

Figures

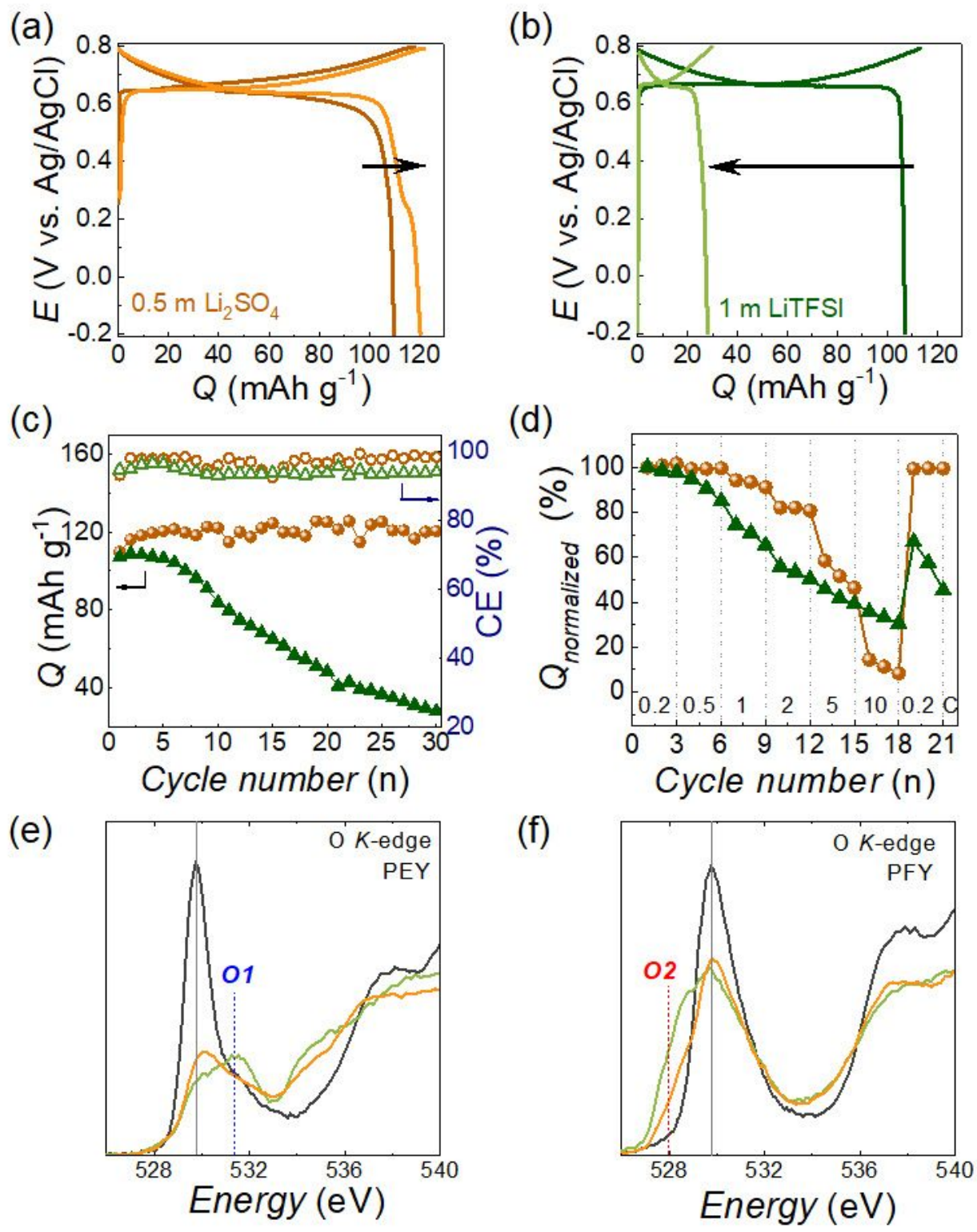


Figure 1

Galvanostatic examinations and X-ray analyses of LCO electrodes with 0.5 m Li₂SO₄ (orange) and 1 m LiTFSI (green). (a–c) Potential profiles of (a) 0.5 m Li₂SO₄ and (b) 1 m LiTFSI for 1st (dark) and 30th cycle (light) at 0.5C, and (c) comparison of capacity retention (Q) and Coulombic efficiency (CE). (d) Rate capability from 0.2C to 10C. (e–f) XAFS analyses of 30th cycled LCO electrodes with 0.5 m Li₂SO₄ (orange) and 1 m LiTFSI (green) and pristine LCO (black) in (e) O K-edge PEY and (f) O K-edge PFY

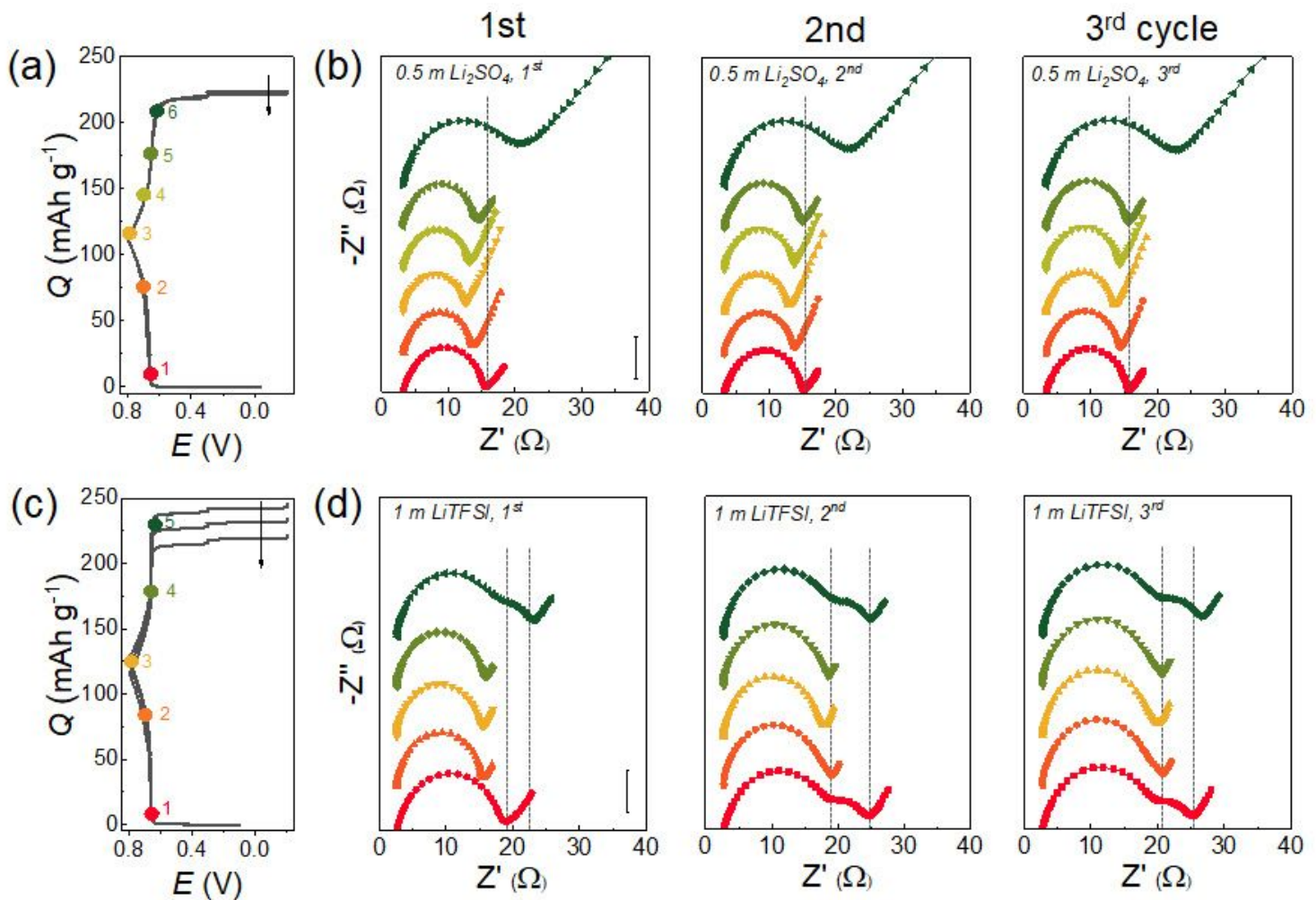


Figure 2

Galvanostatic profiles and corresponding EIS analysis of LCO cells with (a-b) 0.5 m Li_2SO_4 and (c-d) 1 m LiTFSI for consecutive 3 cycles. Nyquist plots in (b) and (d) were acquired after holding for 10 min at the point 1 (red, 0.66 V), 2, (orange, 0.7 V), and 3 (yellow, 0.8 V), and subsequent discharge, 4 (light green, 0.7 V), 5 (green, 0.66 V), and 6 (dark green, 0.63 V, Li_2SO_4 only) in the galvanostatic tests in (a) and (c), respectively. The arrows in (a) and (c) indicate from the 1st to the 3rd cycle. The panels in (b) and (d) correspond to the 1st (left), 2nd (middle), and the 3rd cycle (right). The y-axis scales indicate 5 Ω .

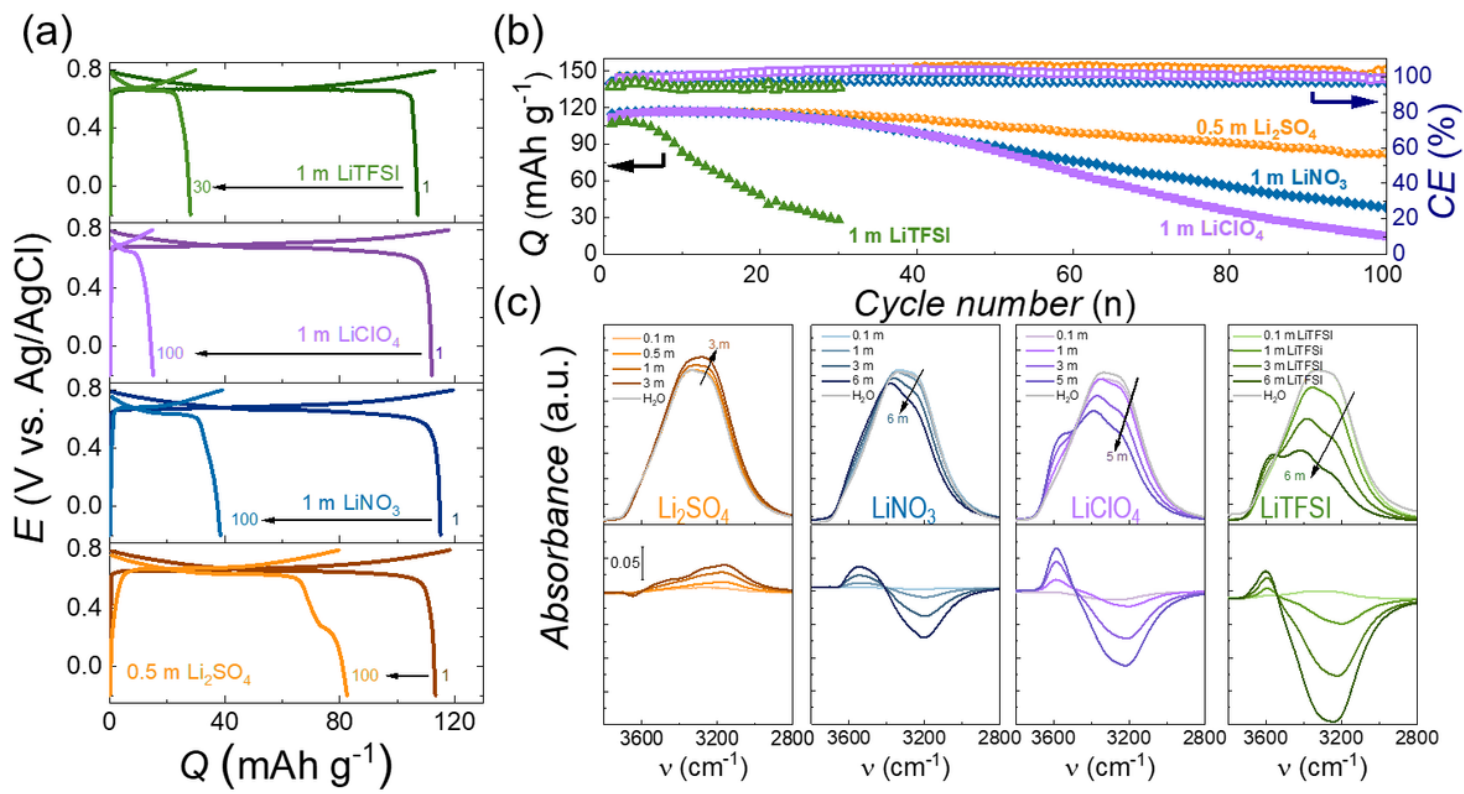


Figure 3

Galvanostatic cycling and ATR-IR analysis with various electrolytes, Li₂SO₄ (orange), LiNO₃ (blue), LiClO₄ (purple), and LiTFSI (green). (a) Potential profiles of LCO at 1st and 100th cycles with 0.5 m Li₂SO₄, 1 m LiNO₃, 1 m LiClO₄, and 1 m LiTFSI (from bottom to top). The potential range was $-0.2 \sim 0.8$ V vs. Ag/AgCl and the current rate was 0.5C. (b) Corresponding capacity retention and CE for 100 cycles. (c) ATR-IR spectra of OH stretching bands (top) and differential signals from pure water (bottom) with increasing electrolyte concentrations.

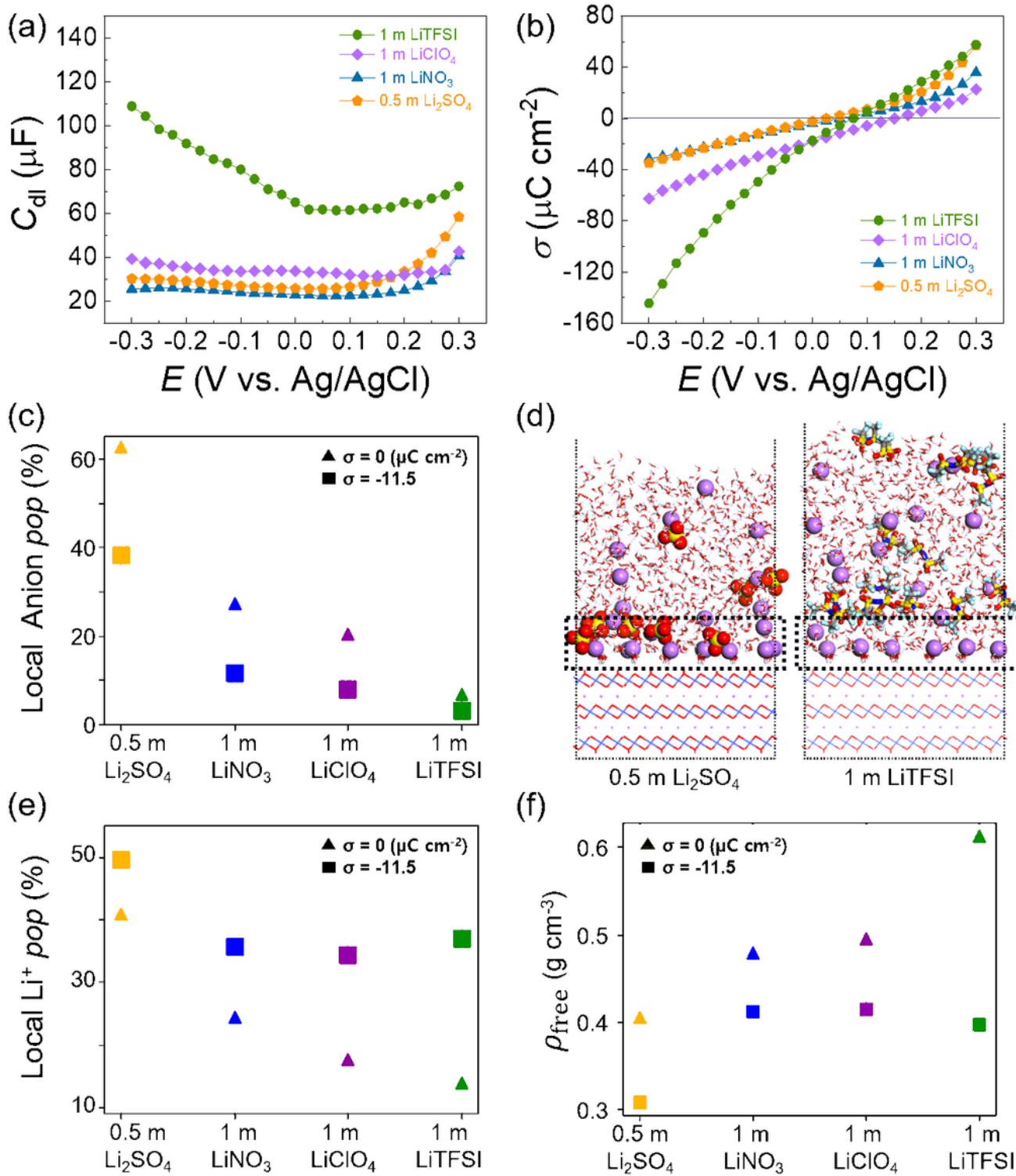


Figure 4

Comparative estimations of the concentration of ions. (a) Electric double-layer capacitance (C_{dl}) measured by stair-case EIS and (b) corresponding surface charge density (σ). Mean-field QM/MM simulation results showing (c) a local anion population (pop), (d) representative structural details when the LCO is cathodically charged by $\sigma = -11.5 \mu\text{C cm}^{-2}$, (e) a local Li⁺ population, and (f) free water density (ρ_{free}) in the interfacial region. Color codes for (d) are; purple for Li⁺, red for O, yellow for S, grey for C,

and cyan for F, Li⁺ and SO₄²⁻ are displayed using spheres while water and LCO are displayed using sticks.

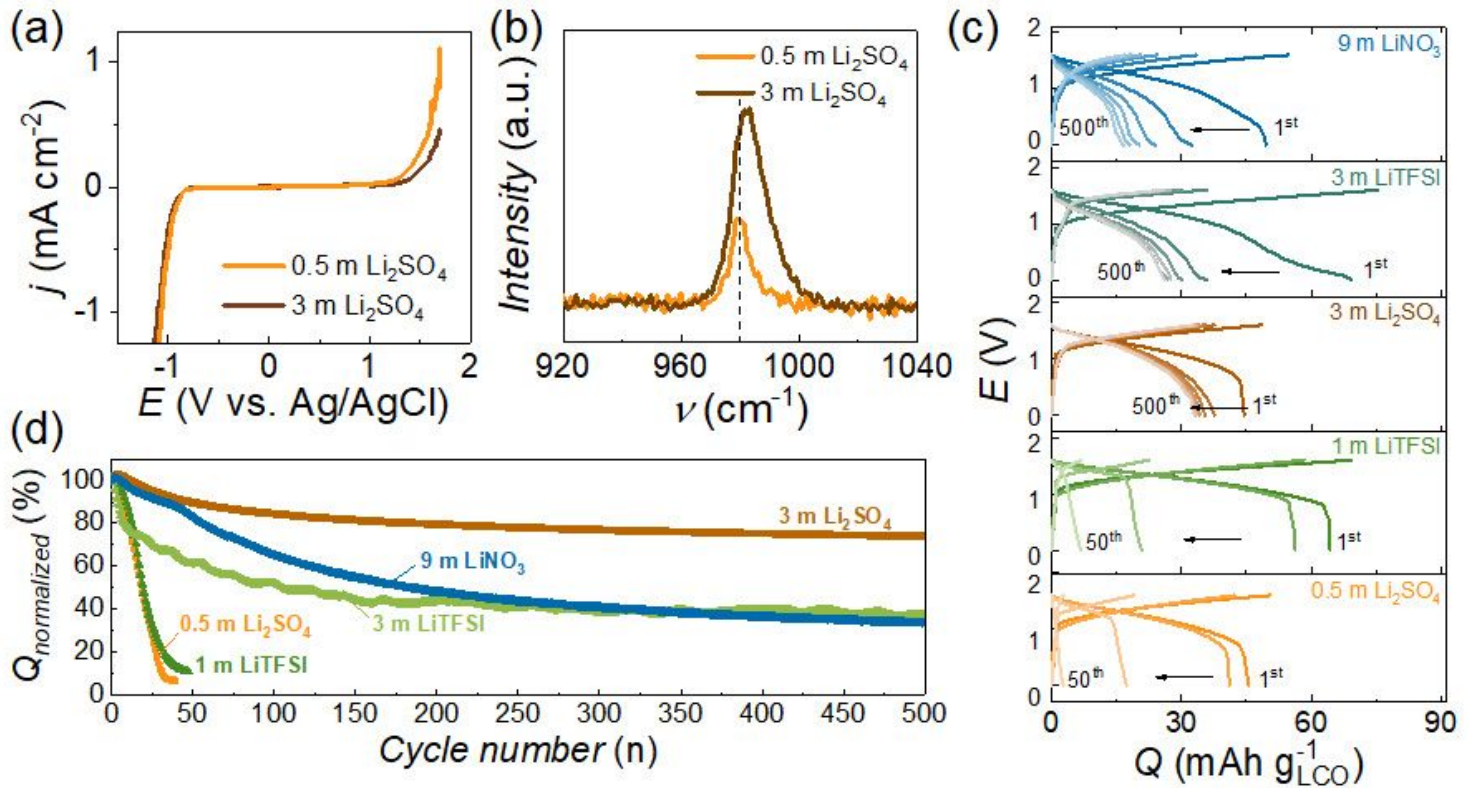


Figure 5

Characterization of high concentration of electrolytes and galvanostatic cycling performance of full cells. (a) Electrochemical potential windows for 0.5 m (orange) and 3 m (brown) Li₂SO₄ at a scan rate of 0.2 mV s⁻¹. (b) Raman spectra of SO₄²⁻ stretching mode with different concentrations. (c) Voltage profiles of full cells with 0.5 m Li₂SO₄, 1 m LiTFSI for 50 cycles, and 3 m Li₂SO₄, 3 m LiTFSI, and 9 m LiNO₃ for 500 cycles (bottom to top). The negative electrode was Li₉/^{7-x}Nb₂/⁷Mo₃/7O₂ (LNMO) and the current rate was 0.5C. (d) Corresponding capacity retention for total 500 cycles.

Supplementary Files

This is a list of supplementary files associated with this preprint. Click to download.

- [OhandShinetalISIsubmission.docx](#)